

MOTT–HUBBARD TRANSITION AND ANDERSON LOCALIZATION: A GENERALIZED DYNAMICAL MEAN-FIELD THEORY APPROACH

*E. Z. Kuchinskii, I. A. Nekrasov, M. V. Sadovskii**

*Institute for Electrophysics, Russian Academy of Sciences
620016, Ekaterinburg, Russia*

Received October 4, 2007

The density of states, the dynamic (optical) conductivity, and the phase diagram of a strongly correlated and strongly disordered paramagnetic Anderson–Hubbard model are analyzed within the generalized dynamical mean-field theory (DMFT+ Σ approximation). Strong correlations are taken into account by the DMFT, and disorder is taken into account via an appropriate generalization of the self-consistent theory of localization. The DMFT effective single-impurity problem is solved by the numerical renormalization group (NRG); we consider the three-dimensional system with a semi-elliptic density of states. The correlated metal, Mott insulator, and correlated Anderson insulator phases are identified via the evolution of the density of states and dynamic conductivity, demonstrating both the Mott–Hubbard and Anderson metal–insulator transition and allowing the construction of the complete zero-temperature phase diagram of the Anderson–Hubbard model. Rather unusual is the possibility of a disorder-induced Mott insulator-to-metal transition.

PACS: 71.10.Fd, 71.27.+a, 71.30.+h

1. INTRODUCTION

The importance of the electron interaction and randomness for the properties of condensed matter is well known [1]. Both Coulomb correlations and disorder are driving forces of metal–insulator transitions (MITs) related to the localization and delocalization of particles. In particular, the Mott–Hubbard MIT is caused by the electron repulsion [2], while the Anderson MIT is due to random scattering of noninteracting particles [3]. Actually, disorder and interaction effects are known to compete in many subtle ways [1, 4]; this problem becomes much more complicated in the case of strong electron correlations and strong disorder, determining the physical mechanisms of the Mott–Anderson MIT [1].

The cornerstone of the modern theory of strongly correlated systems is the dynamic mean-field theory (DMFT) [5–8], constituting a nonperturbative theoretical framework for the investigation of correlated lattice electrons with local interaction. In this approach, the effect of local disorder can be taken into account through the standard average density of states (DOS) [9] in the absence of interactions, leading to

the well-known coherent potential approximation [10], which does not describe the physics of Anderson localization. To overcome this deficiency, Dobrosavljević and Kotliar [11] formulated a variant of the DMFT where the geometrically averaged local DOS was computed from solutions of the self-consistent stochastic DMFT equations. Subsequently, Dobrosavljević et al. [12] incorporated the geometrically averaged local DOS into the self-consistency cycle and derived a mean-field theory of Anderson localization that reproduced many of the expected features of the disorder-driven MIT for noninteracting electrons. This approach was extended in [13] to include Hubbard correlations via the DMFT, which led to a highly nontrivial phase diagram of the Anderson–Hubbard model with the correlated metal, Mott insulator, and correlated Anderson insulator phases. The main deficiency of these approaches, however, is the inability to directly calculate measurable physical properties, such as conductivity, which is of major importance and defines the MIT itself.

At the same time, the well-developed approach of the self-consistent theory of Anderson localization, based on solving the equations for the generalized diffusion coefficient, demonstrated its efficiency in the non-

*E-mail: sadovskii@iep.uran.ru

interacting case a long time ago [14–19]; several attempts to include interaction effects into this approach were made with some promising results [17, 20]. However, until recently, there have been no attempts to incorporate this approach into the modern theory of strongly correlated electron systems. Here, we undertake such a research, studying the Mott–Hubbard and Anderson MITs via direct calculations of both the average DOS and the dynamic (optical) conductivity.

Our approach is based on the recently proposed generalized DMFT+ Σ approximation [21–24], which on the one hand retains the single-impurity description of the DMFT, with a proper account for local Hubbard-like correlations and the possibility to use impurity solvers like the numerical renormalization group (NRG) [25–27], and on the other hand, allows including additional (either local or nonlocal) interactions (fluctuations) on a nonperturbative model basis.

Within this approach, we have already studied both single- and two-particle properties of the two-dimensional Hubbard model, concentrating mainly on the problem of pseudogap formation in the density of states of the quasiparticle band in both correlated metals and doped Mott insulators, with an application to superconducting cuprates. We analyzed the evolution of non-Fermi-liquid-like spectral density and ARPES spectra [22], “destruction” of Fermi surfaces and formation of Fermi “arcs” [21], as well as pseudogap anomalies of optical conductivity [24]. Briefly, we also considered impurity scattering effects [23].

In this paper, we apply our DMFT+ Σ approach for calculations of the density of states, dynamic conductivity, and phase diagram of the strongly correlated and strongly disordered three-dimensional paramagnetic Anderson–Hubbard model. Strong correlations are again taken into account by the DMFT, while disorder is taken into account via the appropriate generalization of the self-consistent theory of localization.

This paper is organized as follows. In Sec. 2, we briefly describe our generalized DMFT+ Σ approximation with application to the disordered Hubbard model. In Sec. 3, we present basic DMFT+ Σ expressions for the dynamic (optical) conductivity and formulate the appropriate self-consistent equations for the generalized diffusion coefficient. Computational details and results for the density of states and dynamic conductivity are given in Sec. 4, where we also analyze the phase diagram of the strongly disordered Hubbard model within our approach. The paper ends with a short summary in Sec. 5 and a discussion of some related problems.

2. BASICS OF THE DMFT+ Σ APPROACH

Our aim is to consider the nonmagnetic disordered Anderson–Hubbard model (mainly) at half-filling for arbitrary interaction and disorder strengths. The Mott–Hubbard and Anderson MITs are investigated on an equal footing. The Hamiltonian of the model is written as

$$H = -t \sum_{\langle ij \rangle \sigma} a_{i\sigma}^\dagger a_{j\sigma} + \sum_{i\sigma} \epsilon_i n_{i\sigma} + U \sum_i n_{i\uparrow} n_{i\downarrow}, \quad (1)$$

where $t > 0$ is the amplitude for hopping between nearest neighbors, U is the on-site repulsion, $n_{i\sigma} = a_{i\sigma}^\dagger a_{i\sigma}$ is the local electron number operator, $a_{i\sigma}$ ($a_{i\sigma}^\dagger$) is the annihilation (creation) operator of an electron with spin σ , and the local ionic energies ϵ_i at different lattice sites are considered independent random variables. To simplify diagrammatics in what follows, we assume the Gaussian probability distribution for ϵ_i :

$$\mathcal{P}(\epsilon_i) = \frac{1}{\sqrt{2\pi}\Delta} \exp\left(-\frac{\epsilon_i^2}{2\Delta^2}\right), \quad (2)$$

where the parameter Δ is a measure of the disorder strength, and a Gaussian (“white” noise) random field of energy level ϵ_i at lattice sites produces “impurity” scattering, leading to the standard diagram technique for calculation on the averaged Green’s functions [19].

The DMFT+ Σ approach was initially proposed in [21–23] as a simple method to include nonlocal fluctuations, of essentially arbitrary nature, into the standard DMFT. In fact, it can be used to include any additional interaction into the DMFT as follows. Working at finite temperatures T , we write the Matsubara–“time” Fourier-transformed single-particle Green’s function of the Hubbard model as

$$G(i\varepsilon, \mathbf{p}) = \frac{1}{i\varepsilon + \mu - \epsilon(\mathbf{p}) - \Sigma(i\varepsilon) - \Sigma_{\mathbf{p}}(i\varepsilon)}, \quad (3)$$

$$\varepsilon = \pi T(2n + 1),$$

where $\epsilon(\mathbf{p})$ is the single-particle spectrum corresponding to the free part of (1), μ is the chemical potential fixed by the electron concentration, $\Sigma(i\varepsilon)$ is the local contribution to self-energy due to the Hubbard interaction, of the DMFT type (surviving in the limit of spatial dimensionality $d \rightarrow \infty$), and $\Sigma_{\mathbf{p}}(i\varepsilon)$ is some additional (in general, momentum-dependent) self-energy part. This last contribution can be caused, e.g., by electron interactions with some “additional” collective modes or order-parameter fluctuations within the Hubbard model itself. But it can actually be due to any other interactions (fluctuations) outside the standard

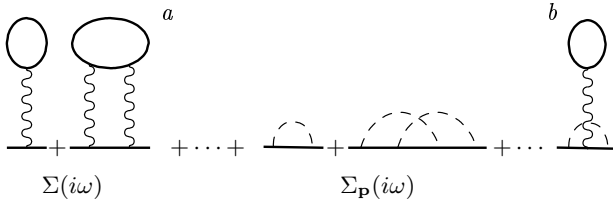


Fig. 1. Typical “skeleton” diagrams for the self-energy in the DMFT+ Σ approach. The first two terms are examples of DMFT self-energy diagrams; the middle two diagrams show contributions due to random impurity scattering represented by dashed lines. The last diagram (b) is an example of a neglected diagram leading to interference between the local Hubbard interaction and impurity scattering

Hubbard model, e.g., due to phonons or random impurity scattering, when it is in fact local (momentum independent). The last interaction is the subject of our main interest in the present paper. The basic assumption here is the neglect of all interference processes of the local Hubbard interaction and “external” contributions due to these additional scatterings (noncrossing approximation for appropriate diagrams) [22], as illustrated by diagrams in Fig. 1.

The self-consistency equations of the generalized DMFT+ Σ approach are formulated as follows [21, 22].

1. Start with some initial guess for the local self-energy $\Sigma(i\varepsilon)$, e.g., $\Sigma(i\varepsilon) = 0$.
2. Construct $\Sigma_{\mathbf{p}}(i\varepsilon)$ within some (approximate) scheme, accounting for interactions with an “external” interaction (impurity scattering in our case), which can in general depend on $\Sigma(i\omega)$ and μ .
3. Calculate the local Green’s function

$$G_{ii}(i\varepsilon) = \frac{1}{N} \sum_{\mathbf{p}} \frac{1}{i\varepsilon + \mu - \epsilon(\mathbf{p}) - \Sigma(i\varepsilon) - \Sigma_{\mathbf{p}}(i\varepsilon)}. \quad (4)$$

4. Define the “Weiss field”

$$\mathcal{G}_0^{-1}(i\varepsilon) = \Sigma(i\varepsilon) + G_{ii}^{-1}(i\varepsilon). \quad (5)$$

5. Using some “impurity solver”, calculate the single-particle Green’s function $G_d(i\varepsilon)$ for the effective Anderson impurity problem, placed at a lattice site i and defined by the effective action that in the obvious notation is written as

$$S_{eff} = - \int_0^\beta d\tau_1 \int_0^\beta d\tau_2 c_{i\sigma}(\tau_1) \mathcal{G}_0^{-1}(\tau_1 - \tau_2) c_{i\sigma}^\dagger(\tau_2) + \int_0^\beta d\tau U n_{i\uparrow}(\tau) n_{i\downarrow}(\tau). \quad (6)$$

In what follows, we use the NRG [25–27] for the “impurity solver”, which allows us to deal also with real frequencies, thus avoiding the complicated problem of analytic continuation from Matsubara frequencies.

6. Define the new local self-energy

$$\Sigma(i\omega) = \mathcal{G}_0^{-1}(i\omega) - G_d^{-1}(i\omega). \quad (7)$$

7. Using this self-energy as the “initial” one in step 1, continue the procedure until (and if) convergence is reached, to obtain

$$G_{ii}(i\varepsilon) = G_d(i\varepsilon). \quad (8)$$

Eventually, we obtain the desired Green’s function in form (3), with $\Sigma(i\varepsilon)$ and $\Sigma_{\mathbf{p}}(i\varepsilon)$ appearing at the end of our iterative procedure.

For $\Sigma_{\mathbf{p}}(i\varepsilon)$ in the random impurity problem, we use the simplest possible one-loop contribution, given by the third diagram in Fig. 1a, neglecting “crossing” diagrams like the fourth in Fig. 1a, i.e., just the self-consistent Born approximation [19], which in the case of Gaussian disorder (2) leads to the usual expression

$$\Sigma_{\mathbf{p}}(i\varepsilon) = \Delta^2 \sum_{\mathbf{p}} G(i\varepsilon, \mathbf{p}) \equiv \Sigma_{imp}(i\varepsilon) \quad (9)$$

which is actually \mathbf{p} -independent (local).

3. DYNAMIC CONDUCTIVITY IN THE DMFT+ Σ APPROACH

A. Basic expressions for optical conductivity

Physically, it is clear that calculations of the dynamic conductivity are the most direct way to study MITs, because its frequency dependence along with the static value at zero frequency of an external field allows clearly distinguishing between metallic and insulating phases (at zero temperature $T = 0$).

To calculate the dynamic conductivity, we use the general expression relating it to the retarded density-density correlation function $\chi^R(\omega, \mathbf{q})$ [14, 19]:

$$\sigma(\omega) = - \lim_{q \rightarrow 0} \frac{ie^2\omega}{q^2} \chi^R(\omega, \mathbf{q}), \quad (10)$$

where e is the electron charge.

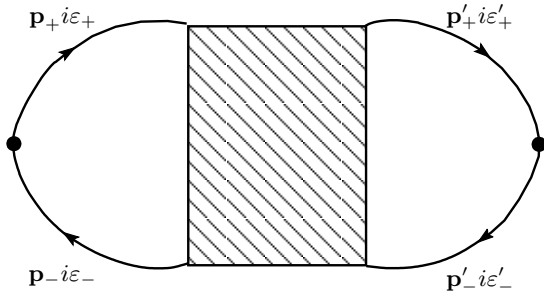


Fig. 2. Full polarization loop with the vertex part describing all interactions and impurity scatterings in the particle–hole channel. The loop without vertex corrections is included implicitly. Here, $\mathbf{p}_\pm = \mathbf{p} \pm \mathbf{q}/2$ and $\varepsilon_\pm = \varepsilon \pm \omega/2$

We next outline the derivation presented in detail in Ref. [24] for the pseudogap problem, with necessary modifications for the present case. We consider the full polarization-loop graph in the Matsubara representation shown in Fig. 2, which is conveniently (with explicit frequency summation) written as

$$\Phi(i\omega, \mathbf{q}) = \sum_{\varepsilon\varepsilon'} \Phi_{i\varepsilon i\varepsilon'}(i\omega, \mathbf{q}) \equiv \sum_{\varepsilon} \Phi_{i\varepsilon}(i\omega, \mathbf{q}) \quad (11)$$

and contains all possible interactions of our model, described by the full shaded vertex part. Actually, we implicitly assume here that the simple-loop contribution without vertex corrections is also included in Fig. 2, which shortens further diagrammatic expressions [24]. The retarded density–density correlation function is determined by an appropriate analytic continuation of this loop and can be written as [14]

$$\chi^R(\omega, \mathbf{q}) = \int_{-\infty}^{\infty} \frac{d\varepsilon}{2\pi i} \{ [f(\varepsilon_+) - f(\varepsilon_-)] \Phi_{\varepsilon}^{RA}(\mathbf{q}, \omega) + f(\varepsilon_-) \Phi_{\varepsilon}^{RR}(\mathbf{q}, \omega) - f(\varepsilon_+) \Phi_{\varepsilon}^{AA}(\mathbf{q}, \omega) \}, \quad (12)$$

where $f(\varepsilon)$ is the Fermi distribution, $\varepsilon_\pm = \varepsilon \pm \frac{\omega}{2}$, and two-particle loops $\Phi_{\varepsilon}^{RA}(\mathbf{q}, \omega)$, $\Phi_{\varepsilon}^{RR}(\mathbf{q}, \omega)$, and $\Phi_{\varepsilon}^{AA}(\mathbf{q}, \omega)$ are determined by the appropriate analytic continuations ($i\varepsilon + i\omega \rightarrow \varepsilon + \omega + i\delta$, $i\varepsilon \rightarrow \varepsilon \pm i\delta$, and $\delta \rightarrow +0$) in (11). Then we can write the dynamic (optical) conductivity as

$$\sigma(\omega) = \lim_{q \rightarrow 0} \left(-\frac{e^2 \omega}{2\pi q^2} \right) \int_{-\infty}^{\infty} d\varepsilon \{ [f(\varepsilon_+) - f(\varepsilon_-)] \times [\Phi_{\varepsilon}^{RA}(\mathbf{q}, \omega) - \Phi_{\varepsilon}^{RA}(0, \omega)] + f(\varepsilon_-) [\Phi_{\varepsilon}^{RR}(\mathbf{q}, \omega) - \Phi_{\varepsilon}^{RR}(0, \omega)] - f(\varepsilon_+) \times [\Phi_{\varepsilon}^{AA}(\mathbf{q}, \omega) - \Phi_{\varepsilon}^{AA}(0, \omega)] \}, \quad (13)$$

where the total contribution of additional terms with zero q can be shown (with the use of general Ward identities) to be zero.

In the DMFT+ Σ approximation, which neglects interference between the local Hubbard interaction and impurity scattering, we calculate $\Phi_{i\varepsilon i\varepsilon'}(i\omega, \mathbf{q})$ entering the sum over Matsubara frequencies in (11) by writing the Bethe–Salpeter equation, shown diagrammatically in Fig. 3, where we introduce the irreducible (local) DMFT vertex $U_{i\varepsilon i\varepsilon'}(i\omega)$ and the “rectangular” vertex containing all interactions with impurities. Analytically, this equation can be written as

$$\Phi_{i\varepsilon i\varepsilon'}(i\omega, \mathbf{q}) = \Phi_{i\varepsilon}^0(i\omega, \mathbf{q}) \delta_{\varepsilon\varepsilon'} + \Phi_{i\varepsilon}^0(i\omega, \mathbf{q}) \sum_{\varepsilon''} U_{i\varepsilon i\varepsilon''}(i\omega) \Phi_{i\varepsilon'' i\varepsilon'}(i\omega, \mathbf{q}), \quad (14)$$

where $\Phi_{i\varepsilon}^0(i\omega, \mathbf{q})$ is the sought function calculated neglecting vertex corrections due to the Hubbard interaction (but taking all interactions due to impurity scattering into account). We note that all the q -dependence is here determined by $\Phi_{i\varepsilon}^0(i\omega, \mathbf{q})$ because the vertex $U_{i\varepsilon i\varepsilon'}(i\omega)$ is local and q -independent.

As we noted in Ref. [24], it is clear from (13) that calculation of the conductivity requires only the knowledge of the q^2 -contribution to $\Phi(i\omega, \mathbf{q})$. This can be easily found as follows. First, we note that all the loops in (14) contain a q -dependence starting from terms of the order of q^2 . Then we can take an arbitrary loop (cross section) in the expansion of (14) (see Fig. 3), calculate it up to terms of the order of q^2 , and make resummation of all contributions to the right and to the left of this cross section, setting $q = 0$ in all these graphs. This is equivalent to simple q^2 -differentiation of the expanded version of Eq. (14). This procedure immediately leads to the following relation for the q^2 -contribution to (11):

$$\phi(i\omega) \equiv \lim_{q \rightarrow 0} \frac{\Phi(i\omega, \mathbf{q}) - \Phi(i\omega, 0)}{q^2} = \sum_{\varepsilon} \gamma_{i\varepsilon}^2(i\omega, \mathbf{q} = 0) \phi_{i\varepsilon}^0(i\omega) \quad (15)$$

with

$$\phi_{i\varepsilon}^0(i\omega) \equiv \lim_{q \rightarrow 0} \frac{\Phi_{i\varepsilon}^0(i\omega, \mathbf{q}) - \Phi_{i\varepsilon}^0(i\omega, 0)}{q^2}, \quad (16)$$

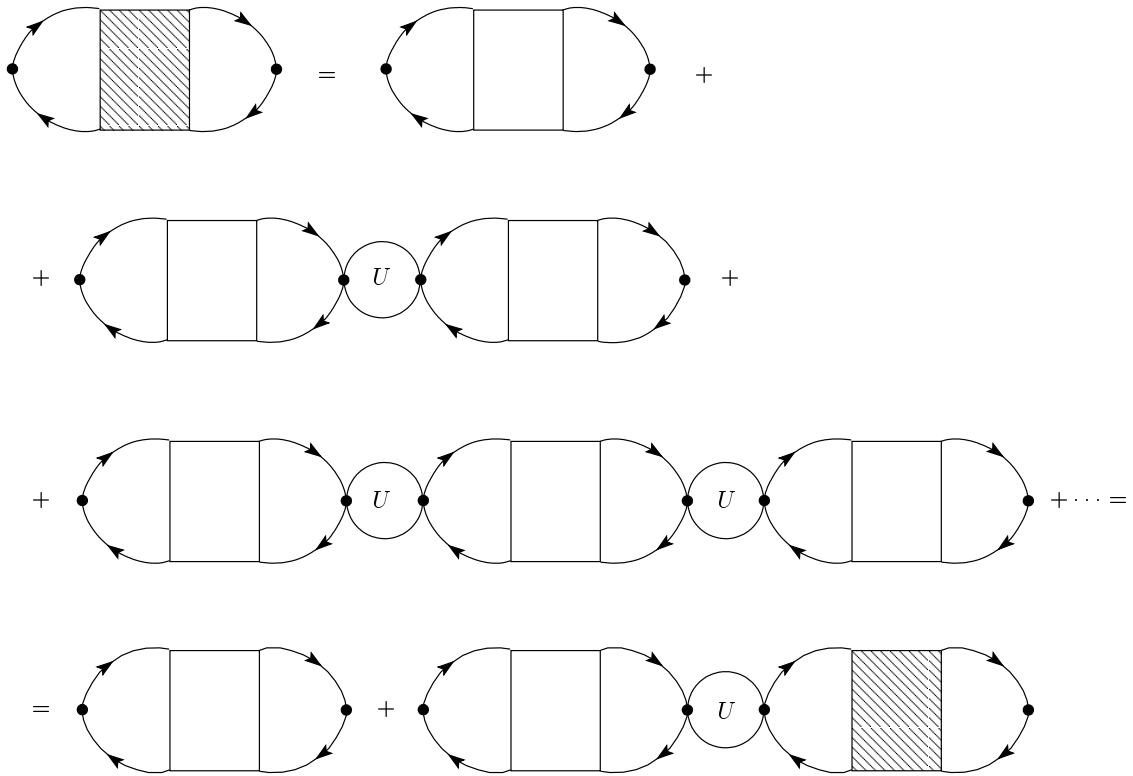


Fig. 3. Bethe-Salpeter equation for the polarization loop in the DMFT+ Σ approach. A circle represents the irreducible vertex part in the particle-hole channel of the DMFT approach, which contains only local Hubbard interactions. An unshaded rectangular vertex represents corrections from impurity scattering only, implicitly including the case of free particle-hole propagation

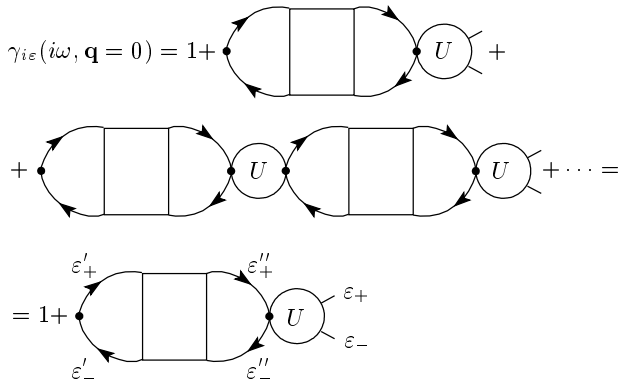


Fig. 4. Effective vertex $\gamma_{i\epsilon}(i\omega, \mathbf{q} = 0)$ used in calculations of conductivity

where $\Phi_{i\epsilon}^0(i\omega, \mathbf{q})$ contains vertex corrections only due to impurity scattering, while the one-particle Green's functions entering it are taken with self-energies due to both impurity scattering and the local DMFT-like interaction, as in Eq. (3). The vertex $\gamma_{i\epsilon}(i\omega, \mathbf{q} = 0)$

is determined diagrammatically as shown in Fig. 4, or analytically as

$$\gamma_{i\epsilon}(i\omega, \mathbf{q} = 0) = 1 + \sum_{\epsilon' \epsilon''} U_{i\epsilon i\epsilon''}(i\omega) \Phi_{i\epsilon'' i\epsilon'}(i\omega, \mathbf{q} = 0). \quad (17)$$

Next, using Bethe-Salpeter equation (14), we can explicitly write

$$\begin{aligned} \gamma_{i\epsilon}(i\omega, \mathbf{q} = 0) &= 1 + \sum_{\epsilon'} \frac{\Phi_{i\epsilon i\epsilon'}(i\omega, \mathbf{q} = 0) - \Phi_{i\epsilon}^0(i\omega, \mathbf{q} = 0)}{\Phi_{i\epsilon}^0(i\omega, \mathbf{q} = 0)} = \\ &= \frac{\sum_{\epsilon'} \Phi_{i\epsilon i\epsilon'}(i\omega, \mathbf{q} = 0)}{\Phi_{i\epsilon}^0(i\omega, \mathbf{q} = 0)}. \quad (18) \end{aligned}$$

At $\mathbf{q} = 0$, we have the following Ward identity, which can be obtained by direct generalization of the proof given in [14, 28] (see the details in the Appendix of Ref. [24]):

$$\begin{aligned}
 (-i\omega)\Phi_{i\varepsilon}(i\omega, \mathbf{q} = 0) &= (-i\omega) \sum_{\varepsilon'} \Phi_{i\varepsilon\varepsilon'}(i\omega, \mathbf{q} = 0) = \\
 &= \sum_{\mathbf{p}} G(i\varepsilon + i\omega, \mathbf{p}) - \sum_{\mathbf{p}} G(i\varepsilon, \mathbf{p}). \quad (19)
 \end{aligned}$$

The denominator in (18) contains vertex corrections only from impurity scattering, while the Green’s functions here are “dressed” by both impurities and the local (DMFT) Hubbard interaction. We can therefore regard the loop entering the denominator as dressed by impurities only, but with the “bare” Green’s functions:

$$\tilde{G}_0(i\varepsilon, \mathbf{p}) = \frac{1}{i\varepsilon + \mu - \epsilon(\mathbf{p}) - \Sigma(i\varepsilon)}, \quad (20)$$

where $\Sigma(i\varepsilon)$ is the local contribution to self-energy from the DMFT. For this problem, we have a Ward identity similar to (19) (see the Appendix in Ref. [24]),

$$\begin{aligned}
 \sum_{\mathbf{p}} G(i\varepsilon + i\omega, \mathbf{p}) - \sum_{\mathbf{p}} G(i\varepsilon, \mathbf{p}) &= \\
 = \Phi_{i\varepsilon}^0(i\omega, \mathbf{q} = 0) [\Sigma(i\varepsilon + i\omega) - \Sigma(i\varepsilon) - i\omega] &\equiv \\
 \equiv \Phi_{i\varepsilon}^0(i\omega, \mathbf{q} = 0) [\Delta\Sigma(i\omega) - i\omega], \quad (21)
 \end{aligned}$$

where we set

$$\Delta\Sigma(i\omega) = \Sigma(i\varepsilon + i\omega) - \Sigma(i\varepsilon). \quad (22)$$

Thus, using (19) and (21) in (18), we obtain the final expression for $\gamma_{i\varepsilon}(i\omega, \mathbf{q} = 0)$ as

$$\gamma_{i\varepsilon}(i\omega, \mathbf{q} = 0) = 1 - \frac{\Delta\Sigma(i\omega)}{i\omega}. \quad (23)$$

Then (15) reduces to

$$\phi(i\omega) = \sum_{\varepsilon} \phi_{i\varepsilon}^0(i\omega) \left[1 - \frac{\Delta\Sigma(i\omega)}{i\omega} \right]^2. \quad (24)$$

Analytic continuation to real frequencies is obvious; using (15) and (24) in (13), we can write the final expression for the real part of dynamic (optical) conductivity as

$$\begin{aligned}
 \text{Re } \sigma(\omega) &= \frac{e^2\omega}{2\pi} \int_{-\infty}^{\infty} d\varepsilon [f(\varepsilon_-) - f(\varepsilon_+)] \times \\
 &\times \text{Re} \left\{ \phi_{\varepsilon}^{0RA}(\omega) \left[1 - \frac{\Sigma^R(\varepsilon_+) - \Sigma^A(\varepsilon_-)}{\omega} \right]^2 - \right. \\
 &\left. - \phi_{\varepsilon}^{0RR}(\omega) \left[1 - \frac{\Sigma^R(\varepsilon_+) - \Sigma^R(\varepsilon_-)}{\omega} \right]^2 \right\}. \quad (25)
 \end{aligned}$$

Thus, we have greatly simplified our problem. To calculate the dynamic conductivity in the DMFT+ Σ

approximation, we only have to solve a single-particle problem as described by the DMFT+ Σ procedure above, this determining self-consistent values of local self-energies $\Sigma(\varepsilon_{\pm})$; while the nontrivial contribution of impurity scattering are to be included via (16), which is to be calculated in some approximation, taking only interaction with impurities (random scattering) into account, but using the “bare” Green’s functions of form (20), which include local self-energies already determined via the general DMFT+ Σ procedure. Actually, (25) also provides an effective algorithm to calculate dynamic conductivity in the standard DMFT (neglecting impurity scattering), because (16) is then easily calculated from a simple loop diagram, determined by two Green’s functions and free scalar vertices. As usual, there is no need to calculate vertex corrections within the DMFT itself, as was first proved considering the loop with vector vertices [7, 8]. Obviously, Eq. (25) effectively interpolates between the case of strong correlations without disorder and the case of pure disorder, without Hubbard correlations, which is of major interest to us. In what follows, we see that calculations based on Eq. (25) give a reasonable overall picture of MIT in the Anderson–Hubbard model.

B. Self-consistent equations for the generalized diffusion coefficient and conductivity

To calculate the optical conductivity, we need to know the basic block $\Phi_{i\varepsilon}^0(i\omega, \mathbf{q})$ entering (16) or, more precisely, the relevant functions analytically continued to real frequencies: $\Phi_{\varepsilon}^{0RA}(\omega, \mathbf{q})$ and $\Phi_{\varepsilon}^{0RR}(\omega, \mathbf{q})$, which in turn define $\phi_{\varepsilon}^{0RA}(\omega)$ and $\phi_{\varepsilon}^{0RR}(\omega)$ entering (25), and are defined by obvious relations similar to (16):

$$\phi_{\varepsilon}^{0RA}(\omega) = \lim_{q \rightarrow 0} \frac{\Phi_{\varepsilon}^{0RA}(\omega, \mathbf{q}) - \Phi_{\varepsilon}^{0RA}(\omega, 0)}{q^2}, \quad (26)$$

$$\phi_{\varepsilon}^{0RR}(\omega) = \lim_{q \rightarrow 0} \frac{\Phi_{\varepsilon}^{0RR}(\omega, \mathbf{q}) - \Phi_{\varepsilon}^{0RR}(\omega, 0)}{q^2}. \quad (27)$$

By definition, we have (with $\mathbf{p}_{\pm} = \mathbf{p} \pm \mathbf{q}/2$)

$$\begin{aligned}
 \Phi_{\varepsilon}^{0RA}(\omega, \mathbf{q}) &= \sum_{\mathbf{p}} G^R(\varepsilon_+, \mathbf{p}_+) G^A(\varepsilon_-, \mathbf{p}_-) \times \\
 &\times \Gamma^{RA}(\varepsilon_-, \mathbf{p}_-; \varepsilon_+, \mathbf{p}_+), \\
 \Phi_{\varepsilon}^{0RR}(\omega, \mathbf{q}) &= \sum_{\mathbf{p}} G^R(\varepsilon_+, \mathbf{p}_+) G^R(\varepsilon_-, \mathbf{p}_-) \times \\
 &\times \Gamma^{RR}(\varepsilon_-, \mathbf{p}_-; \varepsilon_+, \mathbf{p}_+),
 \end{aligned} \quad (28)$$

which are shown diagrammatically in Fig. 5. Here, the Green’s functions $G^R(\varepsilon_+, \mathbf{p}_+)$ and $G^A(\varepsilon_-, \mathbf{p}_-)$

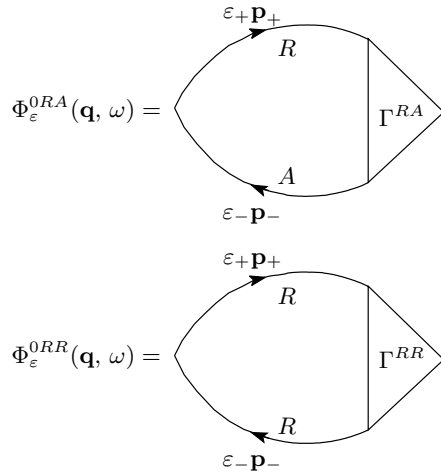


Fig. 5. Diagram representation of $\Phi_\epsilon^{0RA}(\omega, \mathbf{q})$ and $\Phi_\epsilon^{0RR}(\omega, \mathbf{q})$

are defined by analytic continuation ($i\epsilon \rightarrow \epsilon \pm i\delta$) of Matsubara Green's functions (3) determined via our DMFT+ Σ algorithm (4)–(9), while the vertices $\Gamma^{RA}(\epsilon_-, \mathbf{p}_-; \epsilon_+, \mathbf{p}_+)$ and $\Gamma^{RR}(\epsilon_-, \mathbf{p}_-; \epsilon_+, \mathbf{p}_+)$ contain all vertex corrections due to the impurity scattering.

The most important block $\Phi_\epsilon^{0RA}(\omega, \mathbf{q})$ can be calculated using the basic approach of the self-consistent theory of localization [14–19] with appropriate extensions, taking the role of the local Hubbard interaction into account using the DMFT+ Σ approach. The only important difference from the standard approach is that the self-consistent theory equations are derived using the functions

$$G^{R,A}(\epsilon, \mathbf{p}) = \frac{1}{\epsilon + \mu - \epsilon(\mathbf{p}) - \Sigma^{R,A}(\epsilon) - \Sigma_{imp}^{R,A}(\epsilon)}, \quad (29)$$

which contain DMFT contributions $\Sigma^{R,A}(\epsilon)$ in addition to the impurity scattering contained in

$$\begin{aligned} \Sigma_{imp}^{R,A}(\epsilon) &= \Delta^2 \sum_{\mathbf{p}} G^{R,A}(\epsilon, \mathbf{p}) = \\ &= \text{Re} \Sigma_{imp}(\epsilon) \pm i\gamma(\epsilon); \end{aligned} \quad (30)$$

here, $\gamma(\epsilon) = \pi\Delta^2 N(\epsilon)$ and $N(\epsilon)$ is the density of states renormalized by the Hubbard interaction, given in the DMFT+ Σ approach by the usual expression

$$N(\epsilon) = -\frac{1}{\pi} \sum_{\mathbf{p}} \text{Im} G^R(\epsilon, \mathbf{p}). \quad (31)$$

Following all the usual steps of the standard derivation [14–19], we obtain the diffusion-like (at small ω and q) contribution to $\Phi_\epsilon^{0RA}(\omega, \mathbf{q})$ as

$$\Phi_\epsilon^{0RA}(\mathbf{q}, \tilde{\omega}) = \frac{2\pi i N(\epsilon)}{\tilde{\omega} + iD(\omega)q^2}, \quad (32)$$

where an important difference from the single-particle case is contained in

$$\begin{aligned} \tilde{\omega} &= \epsilon_+ - \epsilon_- - \Sigma^R(\epsilon_+) + \Sigma^A(\epsilon_-) = \\ &= \omega - \Sigma^R(\epsilon_+) + \Sigma^A(\epsilon_-) \equiv \omega - \Delta\Sigma^{RA}(\omega) \end{aligned} \quad (33)$$

which replaces the usual ω term in the denominator of the standard expression for $\Phi_\epsilon^{0RA}(\omega, \mathbf{q})$. On general grounds, it is clear that in the metallic phase as $\omega \rightarrow 0$, we have $\Delta\Sigma^{RA}(\omega = 0) = 2i \text{Im} \Sigma(\epsilon) \sim \max\{T^2, \epsilon^2\}$, reflecting Fermi–liquid behavior of DMFT (conserved by elastic impurity scattering). At finite T , this leads to the usual phase decoherence due to electron–electron scattering [1, 4]. The generalized diffusion coefficient $D(\omega)$ is to be determined by solving the basic self-consistency equation introduced below.

Using (32) in (26), we easily obtain

$$\phi_\epsilon^{0RA}(\omega) = \frac{2\pi N(\epsilon)D(\omega)}{\omega^2 \left(1 - \frac{\Delta\Sigma^{RA}(\omega)}{\omega}\right)^2}. \quad (34)$$

Then using (34) in (25) with $\omega \rightarrow 0$ and $T = 0$, we obtain just the usual Einstein relation for the static conductivity:

$$\sigma(0) = e^2 N(0)D(0). \quad (35)$$

All contributions from the Hubbard interaction are reduced to a renormalization of the density of states at the Fermi level and of the diffusion coefficient $D(0)$.

It follows that (25) reduces to

$$\begin{aligned} \text{Re} \sigma(\omega) &= \frac{e^2 \omega}{2\pi} \int_{-\infty}^{\infty} d\epsilon [f(\epsilon_-) - f(\epsilon_+)] \times \\ &\times \text{Re} \left\{ \frac{2\pi N(\epsilon)D(\omega)}{\omega^2} - \right. \\ &\left. - \phi_\epsilon^{0RR}(\omega) \left[1 - \frac{\Delta\Sigma^{RR}(\omega)}{\omega}\right]^2 \right\}, \end{aligned} \quad (36)$$

where the second term can actually be neglected at small ω , or just calculated from (27) with $\Phi_\epsilon^{0RR}(\omega, \mathbf{q})$ given by the usual “ladder” approximation (A.10).

We now formulate our basic self-consistent equation determining the generalized diffusion coefficient $D(\omega)$. We again follow all the usual steps of the self-consistent theory of localization (see the details in the Appendix A), taking the form of our single-particle Green's function (29) into account and not restricting the analysis to the small- ω limit. We can then write the generalized diffusion coefficient as

$$D(\omega) = \frac{\langle v \rangle^2}{d} \frac{i}{\tilde{\omega} + M(\omega)}, \quad (37)$$

where d is the spatial dimensionality and the average velocity $\langle v \rangle$ is defined in (A.6) (to a good approximation, it is just the Fermi velocity). The relaxation kernel $M(\omega)$ satisfies the self-consistency equation, similar to that derived in Refs. [14–19] using “maximally crossed” diagrams for the irreducible impurity scattering vertex (built with Green’s functions (29)):

$$M(\omega) = -\Delta \Sigma_{imp}^{RA}(\omega) + \Delta^4 \sum_{\mathbf{p}} (\Delta G_{\mathbf{p}})^2 \sum_{\mathbf{q}} \frac{1}{\tilde{\omega} + iD(\omega)q^2} \quad (38)$$

with

$$\Delta G_{\mathbf{p}} = G^R(\varepsilon_+, \mathbf{p}) - G^A(\varepsilon_-, \mathbf{p}), \quad (39)$$

and $\Delta \Sigma_{imp}^{RA}(\omega) = \Sigma_{imp}^R(\varepsilon_+) - \Sigma_{imp}^A(\varepsilon_-)$ is due to impurity scattering. It is important to stress once again that there are no contributions to this equation due to vertex corrections determined by the local Hubbard interaction. Using definition (37), we can rewrite Eq. (38) as a self-consistent equation for the generalized diffusion coefficient itself:

$$D(\omega) = i \frac{\langle v \rangle^2}{d} \left\{ \tilde{\omega} - \Delta \Sigma_{imp}^{RA}(\omega) + \Delta^4 \sum_{\mathbf{p}} (\Delta G_{\mathbf{p}})^2 \sum_{\mathbf{q}} \frac{1}{\tilde{\omega} + iD(\omega)q^2} \right\}^{-1} \quad (40)$$

which is to be solved in conjunction with our DMFT+ Σ loop (3)–(9). Due to the limitations of the diffusion approximation, summation over q in (40) is to be restricted to

$$q < k_0 = \min\{l^{-1}, p_F\}, \quad (41)$$

where $l = \langle v \rangle / 2\gamma(0)$ is the elastic mean-free path and p_F is the Fermi momentum [17, 19].

Solving (40) for different sets of parameters of our model and using it in (36) with regular contributions from (A.10), we can calculate the dynamic (optical) conductivity in different phases of the Anderson–Hubbard model.

4. RESULTS AND DISCUSSION

We performed extensive numerical calculations for a simplified version of the three-dimensional Anderson–Hubbard model on a cubic lattice with the semi-elliptic DOS of the “bare” band of width $W = 2D$:

$$N_0(\varepsilon) = \frac{2}{\pi D^2} \sqrt{D^2 - \varepsilon^2}. \quad (42)$$

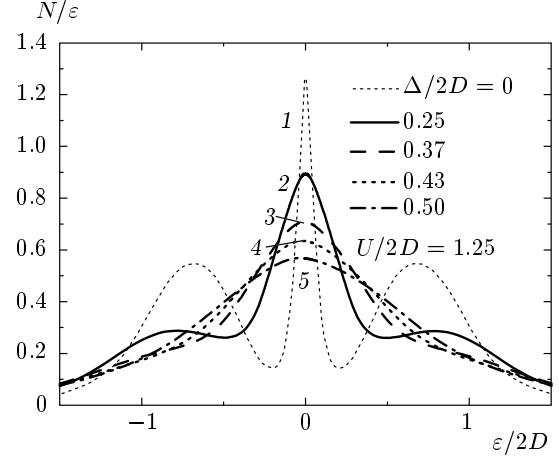


Fig. 6. Density of states of the half-filled Anderson–Hubbard model for different degrees of disorder Δ , and $U = 2.5D$, typical for a correlated metal

The DOS is always given in units of the number of states per energy interval, per lattice cell volume a^3 (a is lattice spacing), and per spin. Some related technical details are given in Appendix B.

We mostly concentrate on the half-filled case, although some results for finite dopings are also presented. The Fermi level is always placed at zero energy.

As the “impurity solver” of DMFT, we used the reliable numerically exact NRG method [25–27]. Calculations were done for temperatures $T \sim 0.001D$, which effectively makes temperature effects in the DOS and conductivity negligible. The discretization parameter of NRG was always $\Lambda = 2$, the number of low-energy states after truncation 1000, the cut-off near Fermi energy [1–6], the broadening parameter $b = 0.6$.

We present only a fraction of most typical results in what follows.

A. Evolution of the density of states

Within the standard DMFT approach, the density of states of the half-filled Hubbard model has a typical three-peak structure: a narrow quasiparticle band (central peak) develops at the Fermi level, with wider upper and lower Hubbard bands forming at $\varepsilon \sim \pm U/2$. The quasiparticle band narrows further with an increase in U in the metallic phase, vanishing at the critical value $U_{c2} \approx 1.5W$, signifying the Mott–Hubbard MIT with a gap opening at the Fermi level [7, 8, 27].

In Fig. 6, we present our DMFT+ Σ results for the density of states, obtained for $U = 2.5D = 1.25W$ typical for a correlated metal without disorder, for different

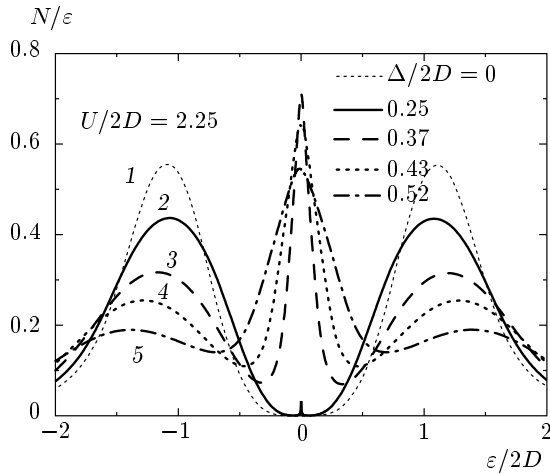


Fig. 7. Density of states of the half-filled Anderson–Hubbard model for different degrees of disorder Δ and $U = 4.5D$, typical for a Mott insulator

degrees of disorder Δ , including large enough values, actually transforming the correlated metal to the correlated Anderson insulator (see subsection 4B). As may be expected, we observe typical widening and damping of the DOS by disorder.

More unexpected are the results obtained for the values of U typical for a Mott insulator without disorder, as shown in Fig. 7 for $U = 4.5D = 2.25W$. We see the restoration of the central peak (quasiparticle band) in the DOS as disorder increases, transforming the Mott insulator to either a correlated metal or a correlated Anderson insulator. Similar behavior of the DOS was recently obtained in Ref. [13]. But in our calculations, the presence of distinct Hubbard bands was already observed for rather large values of disorder, with no signs of vanishing of the Hubbard structure of the DOS, which was observed in Ref. [13]. This is probably due to the very simple nature of our approximation for the DOS under disordering, although we must stress that this difference may be also due to another model of disorder used in Ref. [13] (a flat distribution of ϵ_i in (1) instead of our Gaussian case (2)). Although unimportant, in general, to the physics of Anderson transition, the type of disorder may be significant for the DOS behavior.

It is well known that hysteresis behavior of the DOS is obtained for the Mott–Hubbard transition if DMFT calculations are performed with U decreasing from the insulating phase [8, 27]. The Mott insulator phase survives for the values of U well inside the correlated metal phase, obtained with an increase in U . The metallic phase is restored at $U_{c1} \approx 1.0W$. The values of U in

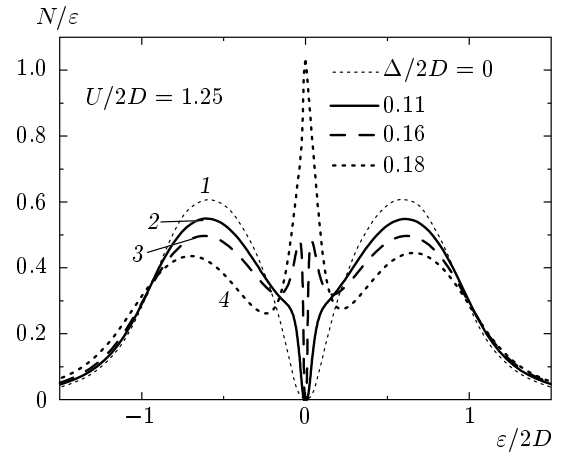


Fig. 8. Restoration of the quasiparticle band by disorder in the coexistence (hysteresis) region for $U = 2.5D$, obtained from a Mott insulator with decreasing U

the interval $U_{c1} < U < U_{c2}$ are usually regarded as belonging to the coexistence region of the metallic and (Mott) insulating phases, with the metallic phase being thermodynamically more stable [8, 27, 29].

In Fig. 8, we present our typical data for the DOS with different disorder for the same value of $U = 2.5D = 1.25W$ as in Fig. 6, but for the hysteresis region, obtained by decreasing U from the Mott insulator phase. We again observe the restoration of the central peak (quasiparticle band) in the DOS under disordering. We also note the peculiar form of the DOS around the Fermi level during this transition: a narrow energy gap is conserved until it is closed by disorder, and a central peak is formed from two symmetric maxima in the DOS merging into the quasiparticle band. This resembles similar behavior observed in the periodic Anderson model [8]. This effect was apparently unnoticed in previous calculations of the DOS in the coexistence region [27] (in the absence of disorder); in our case, it was obtained mainly due to our use of a very fine mesh of values of the disorder parameter Δ .

The physical reason for the rather unexpected restoration of the central (quasiparticle) peak in the DOS is in fact clear. The controlling parameter for its appearance or disappearance in DMFT is actually the ratio of the Hubbard interaction U and the bare bandwidth $W = 2D$. Under disordering, we obtain the new effective bandwidth W_{eff} (in the absence of the Hubbard interaction), which increases with disorder, while the semi-elliptic form of the DOS, with well-defined band edges, is preserved in self-consistent Born approximation (9). This leads to a decrease in the ratio U/W_{eff} , which induces the reappearance of the

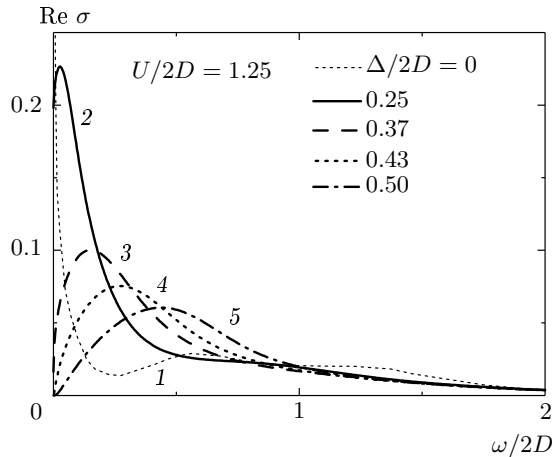


Fig. 9. Real part of dynamic conductivity for the half-filled Anderson–Hubbard model for different degrees of disorder Δ , and $U = 2.5D$, typical for a correlated metal. Lines 1 and 2 are for the metallic phase, line 3 corresponds to the mobility edge (Anderson transition), and lines 4 and 5 correspond to a correlated Anderson insulator

quasiparticle band in our model. This is illustrated in more detail in subsection 4C, where our DOS calculations within the DMFT+ Σ approach for a wide range of parameters are used to study the phase diagram of the Anderson–Hubbard model.

B. Dynamic conductivity: Mott–Hubbard and Anderson transitions

The real part of dynamic (optical) conductivity was calculated for different combinations of the parameters of our model directly from Eqs. (36), (A.9), (A.10), and (40) using the results of DMFT+ Σ loop (3)–(9) as an input. The conductivity values are given below in natural units of $e^2/\hbar a$ (a is the lattice spacing).

In the absence of disorder, evidently, we reproduce the results of the standard DMFT approach [7, 8] with the dynamic conductivity characterized in general by the usual (metallic) Drude-like peak at zero frequency and a wide absorption maximum at $\omega \sim U$, corresponding to transitions to the upper Hubbard band. With an increase in U , the Drude peak decreases and vanishes at the Mott transition, when only transitions through the Mott–Hubbard gap contribute. Introduction of disorder leads to qualitative changes in the frequency dependence of conductivity. In what follows, we mainly show the results obtained for the same values of U and Δ that were used above to illustrate the DOS behavior.

In Fig. 9, we present the real part of dynamic

(optical) conductivity for the half-filled Anderson–Hubbard model for different degrees of disorder Δ , and $U = 2.5D$, typical for a correlated metal. Transitions to the upper Hubbard band at $\omega \sim U$ are practically unobservable in these data. But it can be clearly seen that the metallic Drude peak at zero frequency is widened and suppressed, being gradually transformed into a peak at finite frequencies due to effects of Anderson localization. The Anderson transition occurs at $\Delta_c \approx 0.74D = 0.37W$ (which corresponds to curve 3 in all our graphs, including those for DOS). We note that this value is actually dependent on the value of cutoff (41), which is defined up to a constant of the order of unity [17, 19]. Naive expectations might lead to the conclusion that a narrow quasiparticle band at the Fermi level, which forms in the general case of a highly correlated metal, may be localized much more easily than the typical conduction band. We see, however, that these expectations are wrong and that this band is localized only at strong enough disorder $\Delta_c \sim D$, just as for the whole conduction band of the width $\sim W$. This is in accordance with the previous analysis of localization in a two-band model [30].

More important is the fact that in the DMFT+ Σ approximation, the value of Δ_c is independent of U because all interaction effects enter Eq. (40) only via $\Delta\Sigma^{RA}(\omega) \rightarrow 0$ as $\omega \rightarrow 0$ (at $T = 0$), and hence the interaction drops out at $\omega = 0$. This is actually the main deficiency of our approximation, occurring because we neglect interference effects between the interaction and disorder scattering. An important role of these interference effects has been known for a long time [1, 4]. However, despite the neglect of these effects, we are able to produce physically sound interpolation between two main limits of interest, the pure Anderson transition due to disorder and the Mott–Hubbard transition due to strong correlations. We thus consider it a reasonable first step to the future complete theory of MIT in strongly correlated disordered systems.

In Fig. 10, we present the real part of dynamic (optical) conductivity for different degrees of disorder Δ and $U = 4.5D$, typical for a Mott–Hubbard insulator. In the inset, we show our data for small frequencies, which allow clear distinction of different types of conductivity behavior, especially close to the Anderson transition or in the Mott insulator phase. In this figure, we clearly see the contribution of transitions to the upper Hubbard band at $\omega \sim U$. More importantly, we observe that an increase in disorder produces finite conductivity within the frequency range of the Mott–Hubbard gap, which correlates with the appearance of the quasiparticle band (central peak) in the DOS within

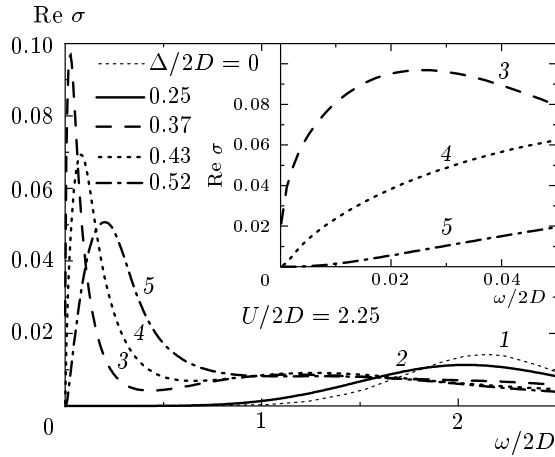


Fig. 10. Real part of dynamic conductivity of the half-filled Anderson–Hubbard model for different degrees of disorder Δ and $U = 4.5D$, typical for a Mott insulator. Lines 1 and 2 correspond to a Mott insulator, line 3 corresponds to the mobility edge (Anderson transition), and lines 4 and 5 are for a correlated Anderson insulator. Inset: the region of low frequencies magnified

this gap, as shown in Fig. 7. In the general case, this conductivity is metallic (finite in the static limit $\omega = 0$) for $\Delta < \Delta_c$; for $\Delta > \Delta_c$, at small frequencies, we obtain $\text{Re}\sigma(\omega) \sim \omega^2$, which is typical of an Anderson insulator [14–19]. We note that due to a finite internal accuracy of NRG numerics, small but finite spurious contributions to $\text{Im}\Sigma^{R,A}(\varepsilon = 0)$ always appear [27] and formally increase with U . These contributions are practically irrelevant in calculations of conductivity in the metallic state. But in an Anderson insulator, these spurious terms contribute via $\tilde{\omega}$ in Eq. (40) and lead to unphysical finite dephasing effects at $\omega = 0$ (or $T = 0$), which can simulate a small finite static conductivity. To eliminate these spurious effects, we had to make appropriate subtractions in our data for $\text{Im}\Sigma^{R,A}(\varepsilon)$ at $\varepsilon = 0$.

Rather unusual is the appearance of a low-frequency peak in $\text{Re}\sigma(\omega)$ even in the metallic phase. It occurs because of weak localization effects, as can be clearly seen from Fig. 11, where we compare the real part of dynamic conductivity for different degrees of disorder Δ and $U = 1.5D$, obtained via our self-consistent approach (taking localization effects into account via “maximally crossed” diagrams) with that obtained using the “ladder” approximation for $\Phi_\varepsilon^{0RA}(\omega, \mathbf{q})$ (similar to (A.10)), which neglects all localization effects. It is clearly seen that in this simple approximation, we just obtain the usual Drude-like peak at $\omega = 0$, while

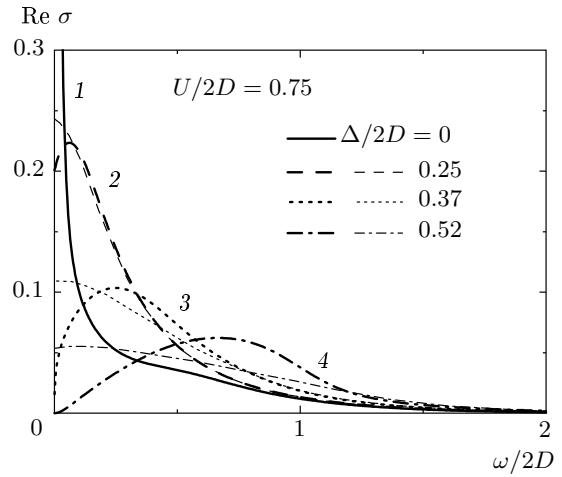


Fig. 11. Real part of dynamic conductivity of the half-filled Anderson–Hubbard model for different degrees of disorder Δ and $U = 1.5D$, comparison of the self-consistent theory (thick lines) with the “ladder” approximation (thin lines)

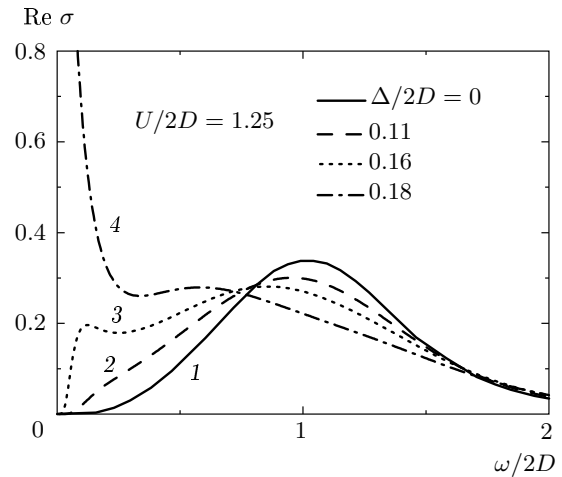


Fig. 12. Real part of dynamic conductivity of the half-filled Anderson–Hubbard model for different degrees of disorder Δ and $U = 2.5D$, obtained from a Mott insulator with decreasing U

accounting for localization effects produces a peak in $\text{Re}\sigma(\omega)$ at low (finite) frequencies. The metallic state is defined [2] by the finite value of zero temperature conductivity at $\omega = 0$.

Up to now, we presented only conductivity data obtained with an increase in U from the metallic to the (Mott) insulating phase. As U decreases from the Mott insulator phase, a hysteresis of conductivity is observed in the coexistence region, defined (in the absence of dis-

order, $\Delta = 0$) by $U_{c1} < U < U_{c2}$. Typical data are shown in Fig. 12, where we present the real part of dynamic conductivity for different degrees of disorder Δ and $U = 2.5D$, obtained from the Mott insulator phase with decreasing U , which should be compared with the data in Fig. 9. Transition to the metallic state via the closure of a narrow gap, “inside” a much wider Mott–Hubbard gap, is clearly seen, which correlates with the DOS data in Fig. 8.

C. Phase diagram of the half-filled Anderson–Hubbard model

The phase diagram of the half-filled Anderson–Hubbard model was studied in Ref. [13] using the approach based on direct DMFT calculations for a set of random realizations of site energies ϵ_i in (1) with subsequent averaging to obtain both the standard average DOS and the geometrically averaged local DOS, which was used to determine the transition to the Anderson insulator phase. Here, we present our results for the zero-temperature phase diagram of the half-filled paramagnetic Anderson–Hubbard model, obtained from extensive calculations of both the average DOS and dynamic (optical) conductivity in the DMFT+ Σ approximation. We note that conductivity calculations are the most direct way to distinguish between metallic and insulating phases [2].

Our phase diagram in the disorder–correlation (Δ, U) plane is shown in Fig. 13. The Anderson transition line $\Delta_c \approx 0.37W = 0.74D$ was determined as the value of disorder for which the static conductivity becomes zero at $T = 0$. The Mott–Hubbard transition can be determined either via the disappearance of the central peak (quasiparticle band) in the DOS or from the conductivity, e.g., from the closure of the gap in the dynamic conductivity in the insulating phase, or from vanishing of the static conductivity in the metallic region. All these methods were used and the corresponding results are shown for comparison in Fig. 13.

We already stressed that the DMFT+ Σ approximation gives the universal (U -independent) value of Δ_c . This is due to a neglect of the interference between disorder scattering and Hubbard interaction, and leads to the main (over)simplification of our phase diagram, compared with that obtained in Ref. [13]. We note that direct comparison of our critical disorder value with those in Ref. [13] is complicated by different types of random site–energy distributions used here (Gaussian) and in Ref. [13] (rectangular). As a rule of thumb (cf. the second reference in [16]), our Gaussian value of Δ_c should be multiplied by $\sqrt{12}$ to obtain the critical

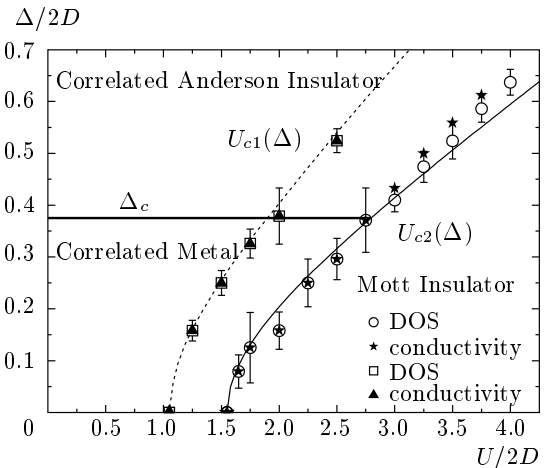


Fig. 13. Zero-temperature phase diagram of the paramagnetic Anderson–Hubbard model. Boundaries of the Mott insulator phase $U_{c1,c2}(\Delta)$ are shown as obtained from Eqs. (45); different symbols show values calculated from either the DOS or the conductivity behavior. The dotted line defines the boundary of the coexistence region obtained with decreasing U from the Mott insulator phase. The Anderson transition line is given by the calculated value of $\Delta_c = 0.37$

disorder value for the rectangular distribution. This gives $\Delta_c \approx 1.28$, in a rather good agreement with the $\Delta_c(U = 0) \approx 1.35W$ value in Ref. [13], justifying our cutoff choice in (41).

The influence of disorder scattering on the Mott–Hubbard transition is highly nontrivial and in some respects is in qualitative agreement with the results in Ref. [13]. The main difference is that our data indicate the survival of Hubbard band structures in the DOS even in the limit of rather large disorder, while these were claimed to disappear in Ref. [13]. Also we obtain the coexistence region smoothly widening with an increase in disorder and not disappearing at a “critical” point, as in Ref. [13]. The borders of our coexistence region, which in fact define the boundaries of the Mott insulator phase obtained with increasing or decreasing U , are determined by the lines $U_{c1}(\Delta)$ and $U_{c2}(\Delta)$ shown in Fig. 13, which are obtained from the simple equation

$$\frac{U_{c1,c2}(\Delta)}{W_{eff}} = \frac{U_{c1,c2}}{W} \tag{43}$$

with

$$W_{eff} = W \sqrt{1 + 16 \frac{\Delta^2}{W^2}}, \tag{44}$$

which is the effective bandwidth in the presence of disorder, calculated for $U = 0$ in self-consistent Born ap-

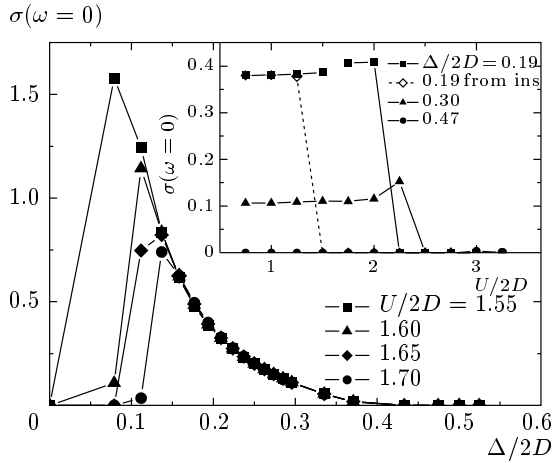


Fig. 14. Disorder dependence of static conductivity, obtained for several values of U and showing a disorder-induced Mott-insulator-to-metal transition. Inset: the static conductivity dependence on U close to the Mott transition, including a typical hysteresis behavior obtained with U decreasing from the Mott insulator phase

proximation (9). Thus, the boundaries of the coexistence region are given by

$$U_{c1,c2}(\Delta) = U_{c1,c2} \sqrt{1 + 16 \frac{\Delta^2}{W^2}}, \quad (45)$$

which are explicitly shown in Fig. 13 by dotted and solid lines, defining the boundaries of the Mott insulator phase. Numerical results for the disappearance of the quasiparticle band (central peak) in the DOS, as well as points following from a qualitative change in the conductivity behavior, are shown in Fig. 13 by different symbols demonstrating very good agreement with these lines, confirming the ratio in (43) as the controlling parameter of the Mott transition in the presence of disorder.

The most striking result of our analysis (also qualitatively demonstrated in Ref. [13]) is the possibility of the metallic state being restored from the Mott–Hubbard insulator with an increase in disorder. This is clear from the phase diagram and is nicely demonstrated by our data for (static) conductivity shown in Fig. 14 for several values of $U > U_{c2}$ and disorder values $\Delta < \Delta_c$. In the inset to Fig. 14, we also illustrate the static conductivity hysteresis observed in the coexistence region of the phase diagram, obtained with U decreasing from the Mott insulator phase.

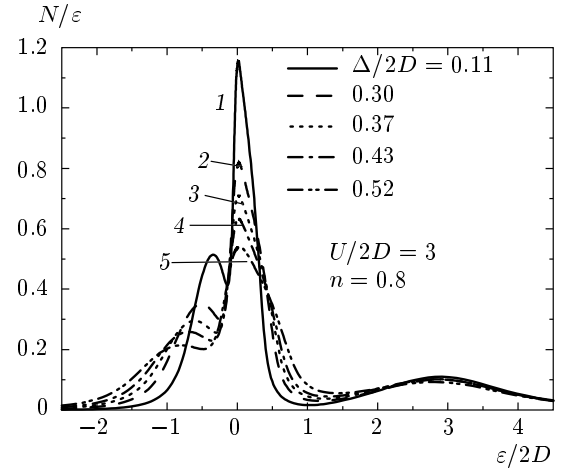


Fig. 15. Density of states of the Anderson–Hubbard model with the electron concentration $n = 0.8$ for different degrees of disorder Δ and $U = 6.0D$, representing the doped Mott insulator

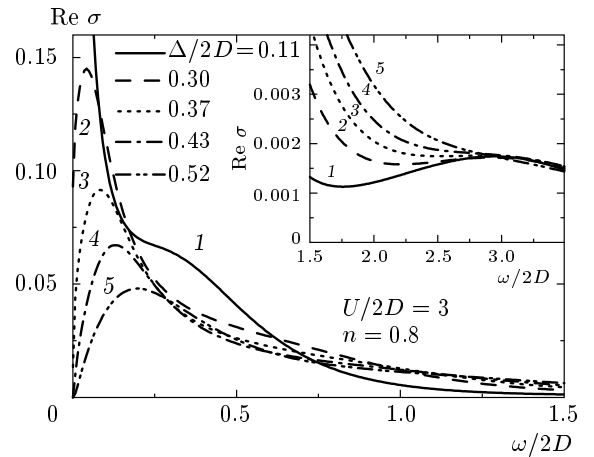


Fig. 16. Real part of dynamic conductivity of the Anderson–Hubbard model with the electron concentration $n = 0.8$ for different degrees of disorder Δ and $U = 6.0D$, representing the doped Mott insulator. Inset: high-frequency behavior with signs of transition to the upper Hubbard band

D. Doped Mott insulator

All results presented above were obtained in the half-filled case. Here, we briefly consider deviations from half-filling. In the metallic phase, doping from half-filling does not produce any qualitative changes in the conductivity behavior, which only demonstrates the Anderson transition with an increase in disorder. We therefore concentrate on the case of a doped Mott insulator. Strictly speaking, in the non-half-filled case, we

never obtain a Mott–Hubbard insulator in the DMFT method at all. In Fig. 15, we show the density of states of the Anderson–Hubbard model with the electron concentration $n = 0.8$ for different degrees of disorder Δ and $U = 6.0D$, representing a typical case of the doped Mott insulator. The quasiparticle band overlaps with the lower Hubbard band and is smeared by disorder, which is just the expected behavior in the metallic state. Nothing spectacular happens to conductivity, either, as is shown for the same set of parameters in Fig. 16. It shows a typical behavior associated with the disorder-induced Anderson MIT. Small signs of transitions to the upper Hubbard band can be seen for $\omega \sim U$ (see the inset to Fig. 16). Therefore, a doped Mott insulator with disorder is qualitatively quite similar to the disordered correlated metal discussed above.

5. CONCLUSION

We used the generalized DMFT+ Σ approach to calculate basic properties of the disordered Hubbard model. The main advantage of our method is its ability to provide a relatively simple interpolation scheme between rather well-understood cases of a strongly correlated system (DMFT and Mott–Hubbard MIT) and of a strongly disordered metal without Hubbard correlations, undergoing an Anderson MIT. Apparently, this interpolation scheme captures the main qualitative features of the Anderson–Hubbard model, such as the general behavior of the DOS and dynamic (optical) conductivity. The overall picture of the zero-temperature phase diagram is also quite reasonable and is in satisfactory agreement with the results of more elaborate numerical work [13]. Actually, our DMFT+ Σ approach is much less time-consuming than more direct numerical approaches, such as that in Ref. [13], and in fact allows calculating all basic (measurable) physical characteristics of the Anderson–Hubbard model.

The main shortcoming of our approach is its neglect of interference effects of disorder scattering and Hubbard interaction, which leads to the independence of the Anderson MIT critical disorder Δ_c from the interaction U . The importance of interference effects is known for a long time [1, 4], but its account was only partially successful in the case of weak correlations. At the same time, the neglect of these interference effects is the major approximation of the DMFT+ Σ method, allowing the derivation of a rather simple and physical interpolation scheme and the analysis of the strong-correlation limit. Attempts to include interference effects in our scheme are postponed for future work.

Another simplification is, of course, our assumption of a nonmagnetic (paramagnetic) ground state of the Anderson–Hubbard model. The importance of magnetic (spin) effects in strongly correlated systems is well known, as is the problem of competition of ground states with different types of magnetic ordering [8]. The importance of disorder in studying the interplay of these possible ground states is also quite evident. These may also be the subject of our future work.

Despite these shortcomings, our results seem very promising, especially concerning the influence of strong disorder on the Mott–Hubbard MIT and the overall form of the phase diagram at zero temperature. The changes in the phase diagram at finite temperatures will be the subject of further studies. Nontrivial predictions of our approach, such as the general behavior of dynamic (optical) conductivity and, especially, the prediction of a disorder-induced Mott-insulator-to-metal transition can be the subject of direct experimental verification.

We are grateful to Th. Pruschke for providing us with his effective NRG code. This work was supported in part by the RFBR grants 05-02-16301 (M. S., E. K., I. N.), 05-02-17244 (I. N.), 06-02-90537 (I. N.), by the joint UrO-SO project (E. K., I. N.), and programs of the Presidium of the Russian Academy of Sciences (RAS) “Quantum macrophysics” and of the Division of Physical Sciences of the RAS “Strongly correlated electrons in semiconductors, metals, superconductors and magnetic materials”. I. N. acknowledges support from the Dynasty Foundation, International Center for Fundamental Physics in Moscow program for young scientists, and from the grant of the President of Russian Federation for young PhD MK-2118.2005.02.

APPENDIX A

Equation for relaxation kernel

We follow the standard approach of the self-consistent theory of localization [14–19], taking the DMFT contributions $\Sigma^{R,A}(\varepsilon)$ into account in single-particle Green’s functions (29) and not restricting ourselves to the usual limit of small ω .

We consider the Bethe–Salpeter equation relating the full two-particle Green’s function $\Phi_{\mathbf{p}\mathbf{p}'}^{0RA}(\omega, \mathbf{q})$ to the irreducible vertex $U_{\mathbf{p}\mathbf{p}'}^{0RA}(\omega, \mathbf{q})$, accounting only for impurity scattering in vertices, but built upon Green’s

functions given by (29). This equation can be written as a generalized kinetic equation in the form [14–19]

$$(\tilde{\omega} - \epsilon(\mathbf{p}) - \Delta \Sigma_{imp}^{RA}(\omega)) \Phi_{\mathbf{p}\mathbf{p}'}^{0RA}(\omega, \mathbf{q}) = -\Delta G_{\mathbf{p}} \times \left(\delta_{\mathbf{p}\mathbf{p}'} + \sum_{\mathbf{p}_1} U_{\mathbf{p}\mathbf{p}_1}^{0RA}(\omega, \mathbf{q}) \Phi_{\mathbf{p}_1\mathbf{p}'}^{0RA}(\omega, \mathbf{q}) \right), \quad (\text{A.1})$$

where $\Delta G_{\mathbf{p}} = G^R(\epsilon_+, \mathbf{p}_+) - G^A(\epsilon_-, \mathbf{p}_-)$. The main difference from a similar equation in Refs. [14–19] is the replacement $\omega \rightarrow \tilde{\omega}$.

We sum both sides of (A.1) and of the same equation multiplied by $\hat{\mathbf{p}} \cdot \hat{\mathbf{q}}$ (where $\hat{\mathbf{p}} = \mathbf{p}/|\mathbf{p}|$ and $\hat{\mathbf{q}} = \mathbf{q}/|\mathbf{q}|$ are appropriate unit vectors) over \mathbf{p} and \mathbf{p}' , with the exact Ward identity [14]

$$\Delta \Sigma_{imp}^{RA}(\omega) = \sum_{\mathbf{p}'} U_{\mathbf{p}\mathbf{p}'}^{0RA}(\omega, \mathbf{q}) \Delta G_{\mathbf{p}'} \quad (\text{A.2})$$

taken into account and with the approximate representation (cf. Ref. [14])

$$\sum_{\mathbf{p}'} \Phi_{\mathbf{p}\mathbf{p}'}^{0RA}(\omega, \mathbf{q}) \approx \frac{\Delta G_{\mathbf{p}}}{\sum_{\mathbf{p}} \Delta G_{\mathbf{p}}} \Phi_{\epsilon}^{0RA}(\omega, \mathbf{q}) + \frac{\Delta G_{\mathbf{p}}(\hat{\mathbf{p}} \cdot \hat{\mathbf{q}})}{\sum_{\mathbf{p}} \Delta G_{\mathbf{p}}(\hat{\mathbf{p}} \cdot \hat{\mathbf{q}})^2} \Phi_{1\epsilon}^{0RA}(\omega, \mathbf{q}), \quad (\text{A.3})$$

where $\Phi_{\epsilon}^{0RA}(\omega, \mathbf{q}) = \sum_{\mathbf{p}\mathbf{p}'} \Phi_{\mathbf{p}\mathbf{p}'}^{0RA}(\omega, \mathbf{q})$ is our loop (28) and $\Phi_{1\epsilon}^{0RA}(\omega, \mathbf{q}) = \sum_{\mathbf{p}\mathbf{p}'} (\hat{\mathbf{p}} \cdot \hat{\mathbf{q}}) \Phi_{\mathbf{p}\mathbf{p}'}^{0RA}(\omega, \mathbf{q})$. An important difference from a similar representation in Refs. [14–19] is that (A.3) is not limited to small ω .

Now (as $q \rightarrow 0$), we obtain the closed system of equations for both $\Phi_{\epsilon}^{0RA}(\omega, \mathbf{q})$ and $\Phi_{1\epsilon}^{0RA}(\omega, \mathbf{q})$,

$$\tilde{\omega} \Phi_{\epsilon}^{0RA}(\omega, \mathbf{q}) - \langle v \rangle q \Phi_{1\epsilon}^{0RA}(\omega, \mathbf{q}) = - \sum_{\mathbf{p}} \Delta G_{\mathbf{p}}, \quad (\text{A.4})$$

$$(\tilde{\omega} + M(\omega)) \Phi_{1\epsilon}^{0RA}(\omega, \mathbf{q}) - \frac{\langle v \rangle}{d} q \Phi_{1\epsilon}^{0RA}(\omega, \mathbf{q}) = 0,$$

where the relaxation kernel is given by

$$M(\omega) = -\Delta \Sigma_{imp}^{RA}(\omega) + \frac{\sum_{\mathbf{p}\mathbf{p}'} (\hat{\mathbf{p}} \cdot \hat{\mathbf{q}}) \Delta G_{\mathbf{p}} U_{\mathbf{p}\mathbf{p}'}^{0RA}(\omega, \mathbf{q}) \Delta G_{\mathbf{p}'} (\hat{\mathbf{p}}' \cdot \hat{\mathbf{q}})}{\sum_{\mathbf{p}} \Delta G_{\mathbf{p}}}, \quad (\text{A.5})$$

with the average velocity $\langle v \rangle$ defined as

$$\langle v \rangle = \frac{\sum_{\mathbf{p}} |\mathbf{v}_{\mathbf{p}}| \Delta G_{\mathbf{p}}}{\sum_{\mathbf{p}} \Delta G_{\mathbf{p}}}; \quad \mathbf{v}_{\mathbf{p}} = \frac{\partial \epsilon(\mathbf{p})}{\partial \mathbf{p}}. \quad (\text{A.6})$$

From (A.4), we immediately obtain that

$$\Phi_{\epsilon}^{0RA}(\mathbf{q}, \tilde{\omega}) = \frac{- \sum_{\mathbf{p}} \Delta G_{\mathbf{p}}}{\tilde{\omega} + iD(\omega)q^2} \quad (\text{A.7})$$

which for small ω reduces to (32) with the generalized diffusion coefficient given by (37).

Using an approximation of “maximally crossed” diagrams for the irreducible vertex $U_{\mathbf{p}\mathbf{p}'}^{0RA}(\omega, \mathbf{q})$ and introducing the standard self-consistency procedure in Refs. [14–19] (i.e., replacing the Drude diffusion coefficient in the Cooperon contribution to the irreducible vertex with the generalized one defined by (37)), we obtain our expression (38) for the relaxation kernel in (A.5).

Our equation (40) for the generalized diffusion coefficient (which is complex in general) reduces just to the usual transcendental equation. It was solved by iterations for each value of $\tilde{\omega}$, taking into account that for $d = 3$ and the cutoff given by (41), the sum entering (40) reduces to

$$\sum_{\mathbf{q}} \frac{1}{\tilde{\omega} + iD(\omega)q^2} = \frac{1}{2\pi^2} \frac{k_0^3}{iD(\omega)k_0^2} \times \int_0^1 \frac{y^2 dy}{y^2 + \frac{\tilde{\omega}}{iD(\omega)k_0^2}} = \frac{1}{2\pi^2} \frac{k_0^3}{iD(\omega)k_0^2} \times \left\{ 1 - \left(\frac{\tilde{\omega}}{iD(\omega)k_0^2} \right)^{1/2} \times \arctg \left(\left(\frac{iD(\omega)k_0^2}{\tilde{\omega}} \right)^{1/2} \right) \right\}. \quad (\text{A.8})$$

For finite frequencies ω , we use $\Phi_{\epsilon}^{0RA}(\mathbf{q}, \tilde{\omega})$ given by (A.7), and hence expression (25) for the dynamic conductivity is to be rewritten as

$$\text{Re } \sigma(\omega) = \frac{e^2 \omega}{2\pi} \int_{-\infty}^{\infty} d\epsilon [f(\epsilon_-) - f(\epsilon_+)] \times \text{Re} \left\{ \frac{i \sum_{\mathbf{p}} \Delta G_{\mathbf{p}} D(\omega)}{\omega^2} - \phi_{\epsilon}^{0RR}(\omega) \left[1 - \frac{\Delta \Sigma^{RR}(\omega)}{\omega} \right]^2 \right\}. \quad (\text{A.9})$$

The second term was here taken in the “ladder” approximation:

$$\Phi_{\epsilon}^{0RR}(\omega, \mathbf{q}) = \frac{\sum_{\mathbf{p}} G^R(\epsilon_+, \mathbf{p}_+) G^R(\epsilon_-, \mathbf{p}_-)}{1 - \Delta^2 \sum_{\mathbf{p}} G^R(\epsilon_+, \mathbf{p}_+) G^R(\epsilon_-, \mathbf{p}_-)}. \quad (\text{A.10})$$

This contribution (nonsingular at small ω) is irrelevant for the conductivity as $\omega \rightarrow 0$, but leads to finite corrections with increasing ω . Equation (A.9) is our final result, which was analyzed numerically in a wide range of frequencies (for small ω , it reduces to (36)).

APPENDIX B

“Bare” electron dispersion and velocity

We consider the “bare” energy band with semi-elliptic DOS (42). Assuming an isotropic electron spectrum $\epsilon(\mathbf{p}) = \epsilon(|\mathbf{p}|) \equiv \epsilon(p)$ and equating the number of states in a spherical layer of momentum space to the number of states in the energy interval $[\epsilon, \epsilon + d\epsilon]$, we obtain a differential equation determining the energy dispersion $\epsilon(p)$:

$$\frac{4\pi p^2 dp}{(2\pi)^3} = N_0(\epsilon) d\epsilon. \quad (\text{B.1})$$

For a quadratic energy dispersion $\epsilon(p)$ close to the lower band edge, we obtain the initial condition for Eq. (B.1) as $p \rightarrow 0$ and $\epsilon \rightarrow -D$. Then we obtain

$$p = \left[6\pi \left(\pi - \varphi + \frac{1}{2} \sin(2\varphi) \right) \right]^{1/3} \quad (\text{B.2})$$

with $\varphi = \arccos(\epsilon/D)$ and the momentum in units of the inverse lattice spacing. Equation (B.2) implicitly defines a “bare” energy dispersion $\epsilon(p)$ for the electronic part of the spectrum $\epsilon \in [-D, 0]$.

For a half-filled band, we easily determine the Fermi momentum as

$$p_F = p(\epsilon = 0) = (3\pi^2)^{1/3}. \quad (\text{B.3})$$

We also need the electron velocity $|\mathbf{v}_\mathbf{p}| = |\partial\epsilon(\mathbf{p})/\partial\mathbf{p}| = \partial\epsilon(p)/\partial p$, which enters expression (A.6) for the average velocity. From (B.1), we obtain

$$|\mathbf{v}_\mathbf{p}| = \frac{d\epsilon}{dp} = \frac{p^2}{2\pi^2} \frac{1}{N_0(\epsilon)}, \quad (\text{B.4})$$

where p is given by Eq. (B.2).

To obtain a quadratic dispersion for the hole part of the spectrum ($\epsilon \in [0, D]$) close to the upper band edge ($\epsilon \rightarrow D$), we introduce the hole momentum $\tilde{p} = 2p_F - p$ and write

$$\frac{4\pi\tilde{p}^2 d\tilde{p}}{(2\pi)^3} = -N_0(\epsilon) d\epsilon \quad (\text{B.5})$$

similarly to (B.1). Letting $\tilde{p} \rightarrow 0$ at the upper band edge $\epsilon \rightarrow 0$, we obtain

$$\tilde{p} = \left[6\pi \left(\varphi - \frac{1}{2} \sin(2\varphi) \right) \right]^{1/3}. \quad (\text{B.6})$$

We then obtain the velocity at the hole part of the spectrum as

$$|\mathbf{v}_\mathbf{p}| = \frac{d\epsilon}{dp} = -\frac{d\epsilon}{d\tilde{p}} = \frac{\tilde{p}^2}{2\pi^2} \frac{1}{N_0(\epsilon)}. \quad (\text{B.7})$$

Equations (B.4) and (B.7) determine the energy dependence of $|\mathbf{v}_\mathbf{p}|$. It is easily seen that the velocity is even in energy and becomes zero at the band edges. These expressions allow passing from momentum summation (e.g., in Eq. (A.6)) to energy integration.

REFERENCES

1. P. A. Lee and T. V. Ramakrishnan, *Rev. Mod. Phys.* **57**, 287 (1985); D. Belitz and T. R. Kirkpatrick, *Rev. Mod. Phys.* **66**, 261 (1994).
2. N. F. Mott, *Proc. Phys. Soc. A* **62**, 416 (1949); *Metal–Insulator Transitions*, 2nd edn., Taylor and Francis, London (1990).
3. P. W. Anderson, *Phys. Rev.* **109**, 1492 (1958).
4. A. M. Finkelshtein, *Sov. Phys. JETP* **75**, 97 (1983); C. Castellani et al., *Phys. Rev. B* **30**, 527 (1984).
5. W. Metzner and D. Vollhardt, *Phys. Rev. Lett.* **62**, 324 (1989).
6. D. Vollhardt, in *Correlated Electron Systems*, ed. by V. J. Emery, World Scientific, Singapore (1993), p. 57.
7. Th. Pruschke, M. Jarrell, and J. K. Freericks, *Adv. Phys.* **44**, 187 (1995).
8. A. Georges, G. Kotliar, W. Krauth, and M. J. Rozenberg, *Rev. Mod. Phys.* **68**, 13 (1996).
9. M. Ulmke, V. Janiš, and D. Vollhardt, *Phys. Rev. B* **51**, 10411 (1995).
10. R. Vlaming and D. Vollhardt, *Phys. Rev. B* **45**, 4637 (1992).
11. V. Dobrosavljević and G. Kotliar, *Phys. Rev. Lett.* **78**, 3943 (1997).
12. V. Dobrosavljević, A. A. Pastor, and B. K. Nikolić, *Europhys. Lett.* **62**, 76 (2003).
13. K. Byczuk, W. Hofstetter, and D. Vollhardt, *Phys. Rev. Lett.* **94**, 056404 (2005).
14. D. Vollhardt and P. Wölfle, *Phys. Rev. B* **22**, 4666 (1980); *Phys. Rev. Lett.* **48**, 699 (1982).
15. P. Wölfle and D. Vollhardt, in *Anderson Localization*, ed. by Y. Nagaoka and H. Fukuyama, Springer Series in Solid State Sciences, Vol. 39, Springer-Verlag, Berlin (1982), p. 26.
16. A. V. Myasnikov and M. V. Sadovskii, *Fiz. Tverd. Tela* **24**, 3569 (1982) [*Sov. Phys.-Solid State* **24**, 2033 (1982)]; E. A. Kotov and M. V. Sadovskii, *Z. Phys. B* **51**, 17 (1983).

17. M. V. Sadovskii, in *Soviet Scientific Reviews—Physics Reviews*, ed. by I. M. Khalatnikov, Vol. 7, Harwood Academic Publ., New York (1986), p. 1.
18. D. Vollhardt and P. Wölfle, in *Electronic Phase Transitions*, ed. by W. Hanke and Yu. V. Kopayev, Vol. 32, North-Holland, Amsterdam (1992), p. 1.
19. M. V. Sadovskii, *Diagrammatics*, World Scientific, Singapore (2006).
20. E. Z. Kuchinskii, M. V. Sadovskii, and V. G. Suvorov. *Zh. Eksp. Teor. Fiz.* **107**, 2027 (1995) [*JETP* **80**, 1122 (1995)]; E. Z. Kuchinskii and M. A. Erkabaev, *Fiz. Tverd. Tela* **39**, 412 (1997).
21. E. Z. Kuchinskii, I. A. Nekrasov, and M. V. Sadovskii, *Pis'ma Zh. Eksp. Teor. Fiz.* **82**, 217 (2005) [*JETP Lett.* **82**, 198 (2005)].
22. M. V. Sadovskii, I. A. Nekrasov, E. Z. Kuchinskii, Th. Prushke, and V. I. Anisimov, *Phys. Rev. B* **72**, 155105 (2005).
23. E. Z. Kuchinskii, I. A. Nekrasov, and M. V. Sadovskii, *Fizika Nizkikh Temperatur* **32**, 528 (2006) [*Low Temp. Phys.* **32**, 398 (2006)].
24. E. Z. Kuchinskii, I. A. Nekrasov, and M. V. Sadovskii, *Phys. Rev. B* **75**, 115102 (2007).
25. K. G. Wilson, *Rev. Mod. Phys.* **47**, 773 (1975); H. R. Krishna-Murthy, J. W. Wilkins, and K. G. Wilson, *Phys. Rev. B* **21**, 1003 (1980); *ibid.* **21**, 1044 (1980); A. C. Hewson, *The Kondo Problem to Heavy Fermions*, Cambridge Univ. Press, Cambridge (1993).
26. R. Bulla, A. C. Hewson and Th. Pruschke, *J. Phys. Condens. Matter* **10**, 8365 (1998).
27. R. Bulla, *Phys. Rev. Lett.* **83**, 136 (1999); R. Bulla, T. A. Costi and D. Vollhardt, *Phys. Rev. B* **64**, 045103 (2001).
28. A. B. Migdal, *Theory of Finite Fermi Systems and Applications to Atomic Nuclei*, Interscience Publishers, New York (1967).
29. N. Blüemer, *Mott-Hubbard Metal-Insulator Transition and Optical Conductivity*, Thesis, München (2002).
30. M. A. Erkabaev and M. V. Sadovskii, *J. Moscow Phys. Soc.* **2**, 233 (1992).

Note added in proff (27 December 2007). Further numerical work has shown that the tendency of $U_{c2}(\Delta)$ data points in Fig. 13 to deviate upwards from the “universal” curve given by Eq. (45) increases for larger values of U , with these data points approaching the $U_{c1}(\Delta)$ curve. However, up to $U/2D \sim 10$, we do not observe the “critical point” discovered in Ref. [13].